Scattered $P'P'$ Waves Observed at Short Distances

by Paul S. Earle, Sebastian Rost, Peter M. Shearer, and Christine Thomas[*]

Abstract   We detect previously unreported 1 Hz scattered waves at epicentral distances between 30° and 50° and at times between 2300 and 2450 s after the earthquake origin. These waves likely result from off-azimuth scattering of *PKPbc* to *PKPbc* in the upper mantle and crust and provide a new tool for mapping variations in fine-scale (10 km) mantle heterogeneity. Array beams from the Large Aperture Seismic Array (LASA) clearly image the scattered energy gradually emerging from the noise and reaching its peak amplitude about 80 s later, and returning to the noise level after 150 s. Stacks of transverse versus radial slowness (ρ_t, ρ_r) show two peaks at about $(2, -2)$ and $(-2, -2)$ s/°, indicating the waves arrive along the major arc path (180° to 360°) and significantly off azimuth. We propose a mantle and surface *PKPbc* to *PKPbc* scattering mechanism for these observations because (1) it agrees with the initiation time and distinctive slowness signature of the scattered waves and (2) it follows a scattering path analogous to previously observed deep-mantle $PK{\bullet}KP$ scattering (Chang and Cleary, 1981). The observed upper-mantle scattered waves and $PK{\bullet}KP$ waves fit into a broader set of scattered waves that we call $P'{\bullet}d{\bullet}P'$, which can scatter from any depth, d, in the mantle.

Introduction

Much of what we know about Earth's internal structure at scale lengths around 10 km comes from teleseismic observations of 1 Hz scattered waves. These waves originate when high-frequency surface or body waves interact with fine-scale volumetric heterogeneity or rough boundary layers. Here we document newly observed teleseismic scattered waves that have the potential to help map the 3D variation of fine-scale scatters in the mantle from core to crust and provide insight into its composition, flow, and partitioning.

Determining the distribution of fine-scale heterogeneity within the Earth's mantle is complicated because strong scattering near its surface dominates most observed scattered waves at teleseismic distances. For example, P, P_{diff}, and S-coda waves primarily originate in the heterogeneous crust and lithosphere (Dainty, 1990; Sato and Fehler, 1998), but also likely contain contributions from deeper in the mantle (Bataille and Lund, 1996; Shearer and Earle, 2004). There are, however, a handful of previously studied probes to fine-scale mantle structure utilizing scattered energy, such as *PKPdf* precursors and scattered *PKKP*, that are more sensitive to deep-mantle structure and arrive in time-distance windows not dominated by contaminating upper-mantle scattering.

PKPdf precursors originate from scattering off fine-scale structure on or above the core-mantle boundary (CMB;

Haddon, 1972). These heterogeneities may extend up to 1000 km above the CMB (Hedlin *et al.*, 1997; Cormier, 1999; Margerin and Nolet, 2003). However, near and above this depth, *PKPdf* precursors are contaminated by interference of the *PKPdf* arrival, complicating their use to study the entire depth of the mantle.

Scattered *PKKP* waves have also been used to study deep-mantle heterogeneity. Two scattering mechanisms associated with this phase have been observed. The first is scattering near the *PKKP* CMB entry and exit points that produce waves seen between about 125° and 135° (Doornbos, 1974). This mechanism is analogous to the origin of *PKPdf* precursors. The second mechanism is scattering near the *PKKP* CMB underside-reflection point as described in Chang and Cleary (1981) and Earle and Shearer (1997). These waves, called $PK{\bullet}KP$, with • indicating the location of the scattering, are caused by off-azimuth scattering of the *PKKPbc* branch and were originally attributed to scattering from a rough CMB. Recent analysis (Earle, 2002; Rost and Earle, 2010) show though that $PK{\bullet}KP$ originates from volumetric scattering in the D'' region. Theoretically, $PK{\bullet}KP$ waves can arrive between 0° and the *PKKP* b-caustic at about 125°, although most observations are at distances larger than 20° (Earle, 2002; Rost and Earle, 2010). As will be discussed, $PK{\bullet}KP$ is closely related to the upper-mantle scattered waves described in this paper.

Here we document scattered waves arriving late in the teleseismic wave field between 30° and 50°. We show that

*Previously at the Department of Earth and Ocean Sciences, University of Liverpool, UK.

off-azimuth scattering of *PKPbc* to *PKPbc* in the upper mantle by a mechanism analogous to *PK•KP* scattering explains the main features of these previously unknown waves. The waves hold promise for future development of both 1D scattering profiles and 3D maps of fine-scale heterogeneity.

Data and Processing

We examine a quiet window of the high-frequency teleseismic wave field between 2200 and 2500 s after the event origin time and between 30° and 50° epicentral distance. Figure 1 shows the study window along with possibly contaminating body waves that include *SKKSdf*, *PKPPKPdf* (*P′P′df*), and four branches of *PKKKP*. This time window is well removed from the contaminating effects of the main *P*-wave coda.

We use data from the Large Aperture Seismic Array (LASA). LASA was operated near Billings, Montana, from 1968 to 1978 (Green *et al.*, 1965; Hedlin *et al.*, 2000); throughout most of its lifespan, it consisted of about 350 short-period ∼1 Hz borehole vertical component sensors spread across 200 km. However, due to travel-time anomalies and waveform distortion known to exist for the outer subarrays, our stacks exclude LASA's outer rings, leaving at most 207 stations per event. Earthquake recordings were chosen based on the *P′P′df* signal-to-noise ratio; only large events with depths less than 65 km are used to avoid complications introduced by depth phases. Table 1 lists the hypocentral parameters for the 10 earthquakes and 2 nuclear tests used

in this paper; Figure 2 maps their locations (see Data and Resources).

Array processing offers two main advantages over single-station analysis. First, by averaging the waveforms the incoherent noise is reduced by roughly the square root of the number of recordings. Second, the radial and transverse slowness of an arrival can be determined by applying time shifts and averaging the seismograms (e.g., Rost and Thomas, 2002). This process is known as stacking or beam forming. The radial and transverse slownesses are directly related to the horizontal slowness and arrival azimuth and provide strong constraints on the ray path of an observed seismic wave. There are several ways to display array-processed data. Here we investigate scattered arrivals using array beams that show wave amplitude versus time averaged over a specific slowness range and slowness images that show wave amplitude as a function of radial and transverse slowness averaged over a specific time window.

We begin our stacking procedure by filtering the seismograms to a narrow high-frequency band that produces the highest signal-to-noise ratio for the detected scattered arrivals (0.9 to 2.1 Hz). This high-frequency band might also help to reduce effects of interfering standard phases such as *PKPPKP* (Tkalčić *et al.*, 2006). Then, after removing traces contaminated with data glitches, array beams are generated by coherently stacking the seismograms that have been time shifted to focus energy arriving at a given radial (ρ_r) and transverse (ρ_t) slowness. The time shift added to a given seismogram is equal to $\tau_{cor} - (\rho_r\delta_r + \rho_t\delta_t)$, where τ_{cor} is the station correction for steeply arriving rays from Engdahl and Felix (1971), and δ_r and δ_t are the distance from the center of the array in the radial and transverse directions. In these coordinates, waves traveling less than 180° will have a positive ρ_r, and off-azimuth arrivals will have a nonzero ρ_t.

Data cubes consisting of individual array beams at equally spaced radial and transverse slownesses are generated for each event. The envelope function (positive outline; Kanasewich, 1981) of each array beam is taken and smoothed with a half-second running average. Array beams for specific slowness windows are calculated by averaging the beam envelopes over a desired slowness range. Slowness images are produced by averaging the envelopes over a desired time window. These array beams and slowness images are used to determine the onset time, slowness, and duration of the scattered waves.

Observations

The array beams and slowness images presented in Figures 3 and 4 for the 12 events in Table 1 clearly show previously undocumented scattered waves. The events are arranged in order of decreasing epicentral distance. The event depth, back-azimuth, and epicentral distance are shown in the upper left of the beam plots. The events are labeled A through L, corresponding to the event identification labels in Table 1.

Figure 1. Time-distance window for study (dashed rectangle). Possibly contaminating body waves that cross this window include *SKKSdf*, *P′P′df*, and four branches of *PKKKP*. The only body waves visible in the high-frequency LASA stacks are *PKKKPab* and *PKKKPbc*.

Table 1
Earthquakes and Nuclear Tests Used in This Study

Label*	Origin Time yyyy/mm/dd, hh:mm:ss	Latitude (°)	Longitude (°)	Depth (km)	M_b	Distance (°)
A	1972/09/08, 11:34:44	71.256	−10.565	1.0	5.9	48.4
B	1971/11/06, 22:00:00	51.470	179.110	0.0	6.8	47.2
C	1969/10/02, 22:06:00	51.420	179.190	0.0	6.4	47.2
D	1974/10/16, 05:45:11	52.414	−32.035	27.8	5.7	46.5
E	1973/06/15, 12:10:00	51.093	−179.383	16.5	5.8	46.5
F	1972/08/12, 09:42:07	51.129	−179.275	33.5	5.8	46.4
G	1971/01/25, 16:08:18	51.271	−177.717	48.3	5.9	45.4
H	1973/05/29, 06:14:23	53.740	−163.706	28.6	6.1	36.6
I	1971/08/20, 21:36:11	13.191	−92.447	30.8	5.8	35.3
J	1974/04/06, 03:56:03	54.860	−160.518	41.6	6.0	34.5
K	1974/03/29, 21:50:37	57.328	−153.926	41.9	5.8	30.6
L	1972/08/23, 08:47:18	58.014	−153.494	66.3	5.5	30.4

*The label is used as the event reference in Figures 2, 3, and 4. Most of the events are earthquakes, except events B and C, which are two large underground nuclear tests conducted by the United States: Cannikin (Event B) and MILROW (Event C).
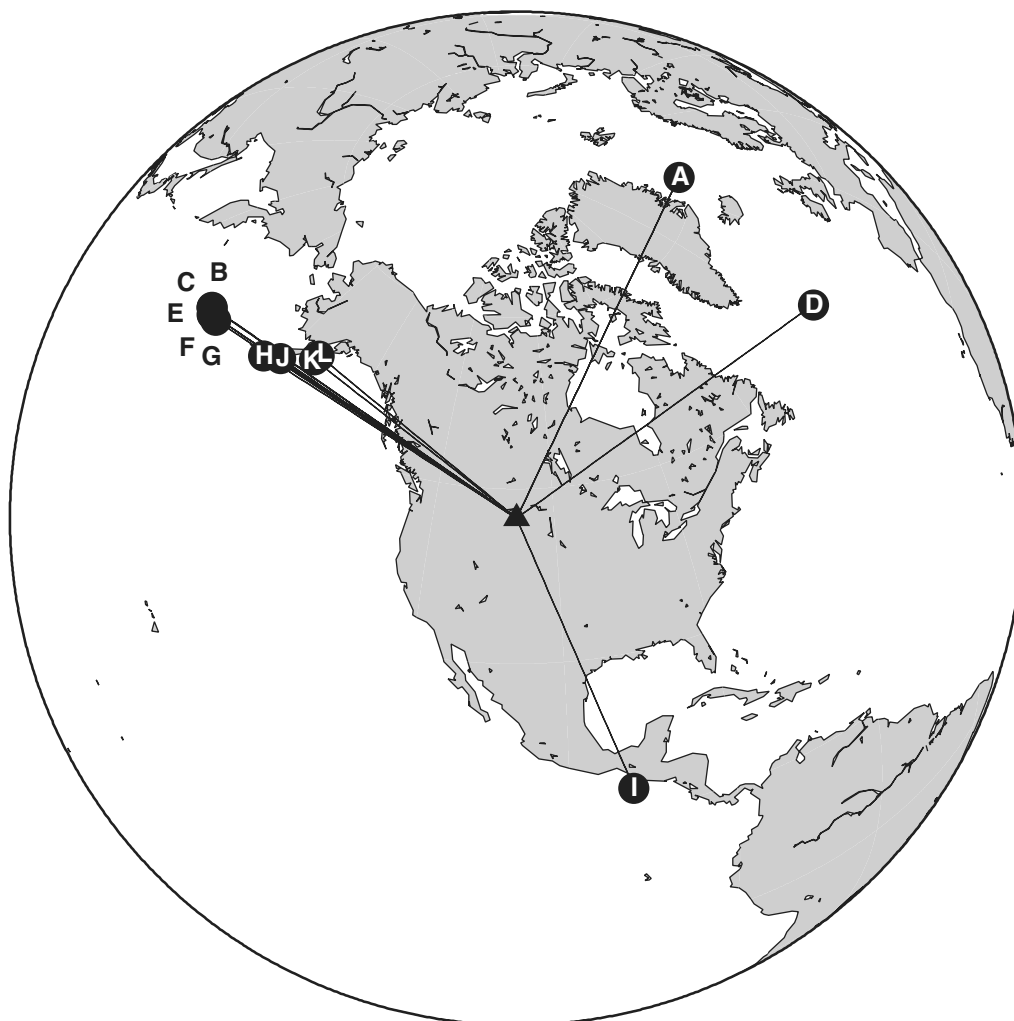
Figure 2. Map of the 10 earthquakes and 2 nuclear explosions used in this paper. The majority of the events are located near the Aleutian Islands. However, the two events in the North Atlantic and one off the coast of Guatemala provide reasonable azimuthal sampling. The letters correspond to the events listed in Table 1.
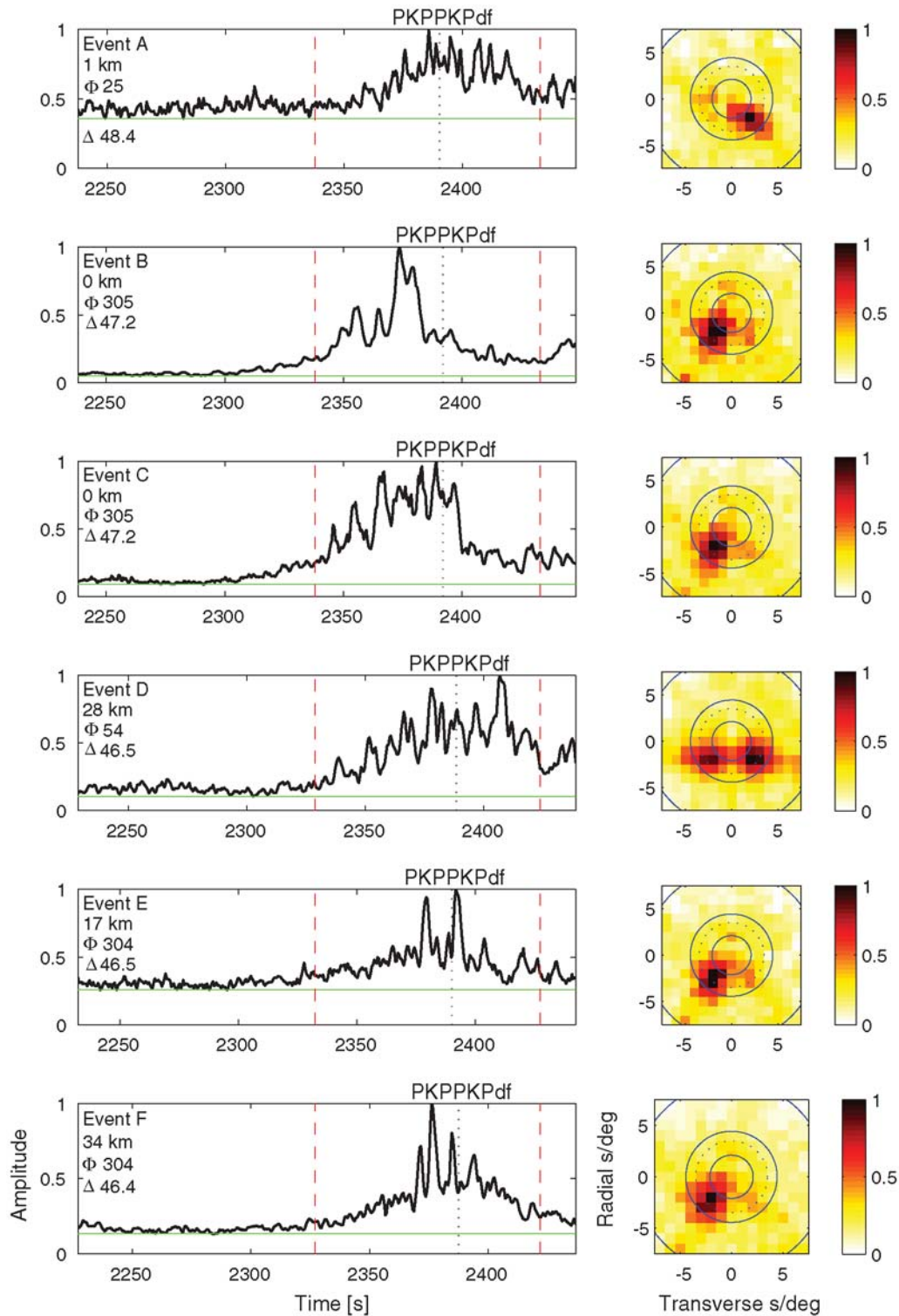
Figure 3. Array beams and slowness images of scattered $P' \bullet d \bullet P'$ waves. The array beams, shown as black lines, are normalized to unit amplitude; the minimum amplitude of the beam envelopes are marked by a green line to indicate the background noise level. The beams are displayed in order of decreasing distance and are labeled corresponding to the entries in Table 1. The slowness images (right) show the distinctive off-azimuth slowness signature of the waves for the time window between the dashed red lines. See text for further details.

The array beams, shown as black lines in the plots on the left, are focused to include energy with radial and transverse slownesses between −5 and 5 s/°. They are normalized to unit amplitude; the minimum amplitudes of the beam envelopes are marked by a green line to indicate the background noise level. The scattered waves begin to rise above the noise at about 2300 s, reach their peak between 2370 and 2400 s, then gradually decrease in amplitude by
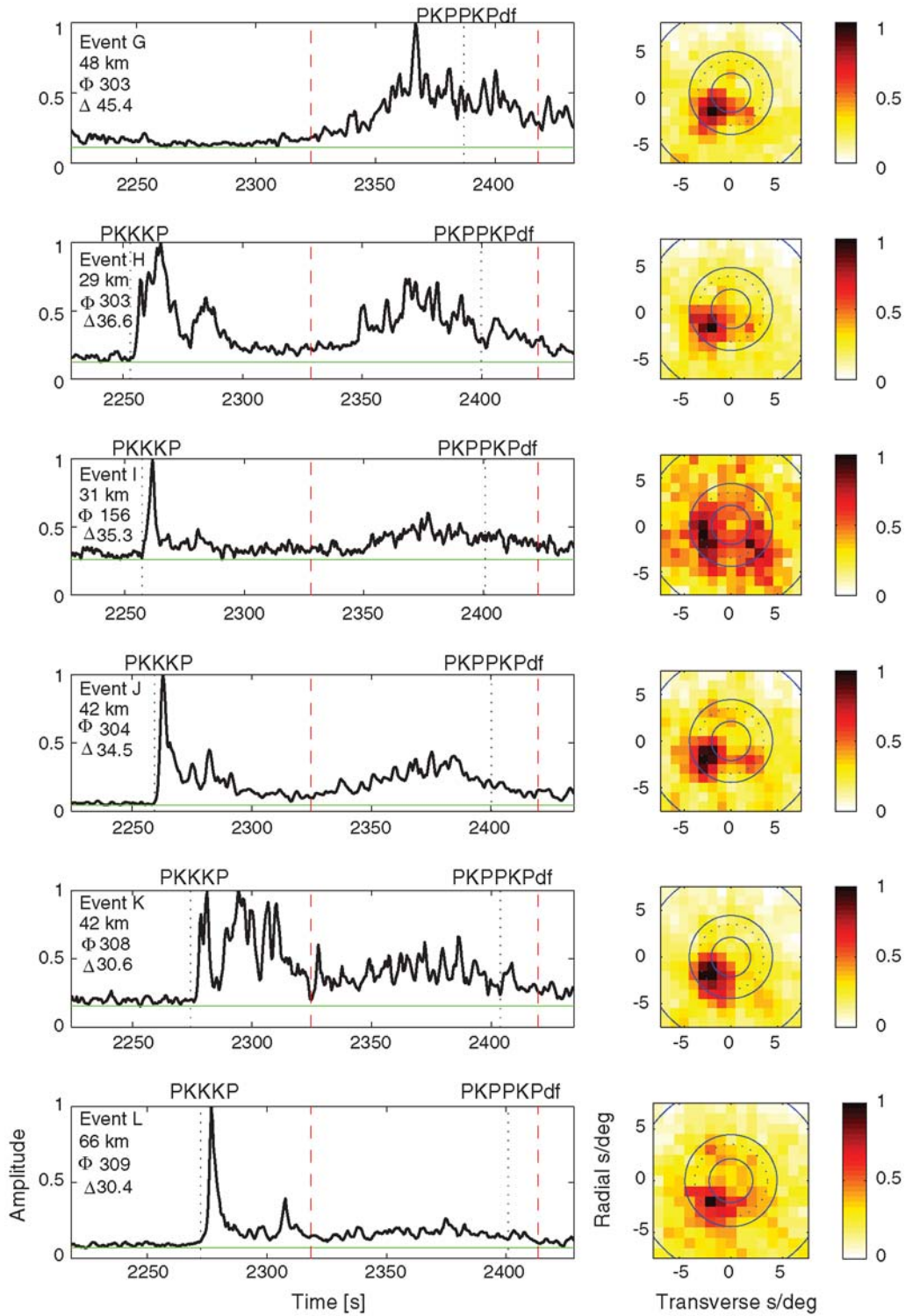
Figure 4.   Array beams and slowness images of scattered $P' \cdot d \cdot P'$ waves. See caption for Figure 3 for details.

about 2450 s. Events A through G contain no other observed arrivals in this time-slowness window, but *PKKKP* and its associated depth phases are clearly seen preceding the scattered waves in events H through L. From the beam traces we do not see evidence for the arrival of *PKPPKPdf* as predicted in these time windows (marked by dotted line).

This might be due to the combined effect of inner-core and upper-mantle attenuation and the general weakness of *PKPPKPdf* in the frequency band used (Tkalčić *et al.*, 2006). Because of contamination from *PKKKP* and its coda at distances less that 30°, observing possible scattered $P'P'$ is difficult.

The slowness images on the right sides of Figures 3 and 4 show the slownesses in seconds per degree of the scattered waves arriving in the time window between the dashed red lines drawn on the beams to the left. One or two slowness peaks are clearly visible in each of the images near $(\rho_t, \rho_r) = (2, -2)$ and/or $(-2, 2)$ amplitude peak near $(-2, -2)$. The majority of these (B, C, E, F, G, H, and J) also have a small secondary peak near $(2, -2)$. Events A and D occurred in the North Atlantic and have large amplitude peaks near $(2, -2)$, while event D has a strong secondary peak near $(-2, -2)$. Finally, the scattered waves generated by the event off the southern coast of Guatemala (I) has a low signal-to-noise ratio, but peaks near $(2, -2)$ and $(-2, -2)$ are visible and of similar amplitude.

The distinctive two-peaked slowness pattern places strong constraints on the origin of the scattered waves. First, the waves' negative radial slowness indicates they travel the major arc path ($180°$ to $360°$) to the station. Second, their nonzero transverse slowness indicates they digress significantly from the great-circle path.

Another notable feature of the array beams is the lack of observed direct $P'P'df$ arrivals in the high-passed LASA data. The predicted $P'P'df$ arrival times are shown as black dotted lines in the array beams of Figures 3 and 4. Although, some peaks in the observed wavetrain arrive near this time (for example, see event E), they do not have $P'P'df$ slownesses, that is, they do not arrive along a great-circle path. The absence of high-frequency $P'P'df$ is not surprising at this range because of high attenuation in the inner core or in the upper mantle during the $P'P'df$ surface reflection. Also absent from the stacks are on-azimuth $PKKKPcd$ and $PKKKPdf$ arrivals.

There exists a danger of falsely interpreting the observed off-azimuth scattered waves as $P'P'df$ in array beams focused only for on-azimuth arrivals ($\rho_t = 0$ s/°). Potentially, an on-azimuth beam could be contaminated by side lobes of off-azimuth arrivals. An off-azimuth arrival's horizontal slowness, $\rho = \mathrm{sqrt}(\rho_t^2 + \rho_r^2)$, will be underestimated if read solely from beams made at $\rho_t = 0$ s/° (Rost and Thomas, 2002, 2009). The off-azimuth energy projects from its true position at (ρ_t, ρ_r) directly onto the radial slowness axis. This results in low estimates of ρ close to the predicted $P'P'df$ slowness.

Origin of Scattered Waves

We propose the observed waves originate from off-azimuth scattering of $PKPbc$-to-$PKPbc$ in Earth's crust and upper mantle with possible contributions from surface scattering near the bounce point. To help visualize the somewhat complex path, Figure 5 illustrates the ray path of this scattered phase. The scattered waves leave the source A, travel as $PKPbc$ to their scattering point in the upper mantle, B, where they scatter to angles outside the source-receiver diametrical plane and travel as $PKPbc$ to the receiver C. Note that the set of possible ray paths is symmetric, so another similar path lies on the other side of the source-receiver diametrical plane creating the two-maxima pattern clearly visible in events D, I, and J.

Theoretically, the scattering point, B, could occur at any depth in the mantle. We use the nomenclature $P' \bullet d \bullet P'$ where d denotes the depth of scattering, $\bullet$ (dot) implies scattering, and P' is the common abbreviation for PKP. So, for example, scattering occurring near the base of the crust is
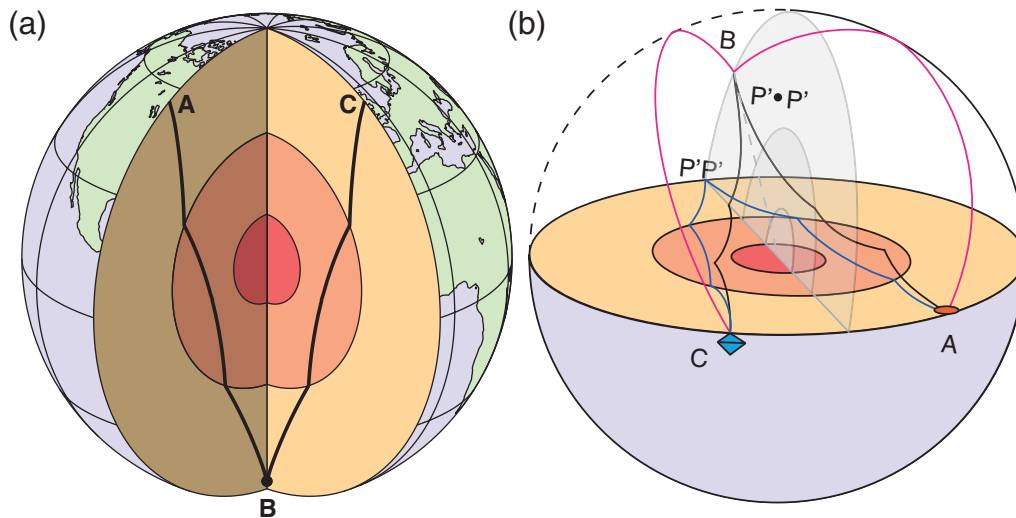
Figure 5. Two representations of the proposed scattering path for observed scattered waves. In both images, the scattered waves leave the source A, travel as $PKPbc$ to their scattering point in the mantle, B, where they scatter to nonspecular angles outside the source-receiver diametrical plane and travel as $PKPbc$ to the receiver, C. (a) The diagram shows a wedge slice into the earth containing the $P' \bullet d \bullet P'$ ray path, and (b) shows both the great-circle $P'P'$ ray path (dark blue) and the out of plane $P' \bullet d \bullet P'$ ray path (black). Note that a symmetric scattering point to B lies on the other side of the source-receiver diametrical plane.

called $P' \cdot 35 \cdot P'$, and scattering at the Earth's surface is called $P' \cdot 0 \cdot P'$ or equivalently $P' \cdot P'$.

We propose the $P' \cdot d \cdot P'$ mechanism because (1) it agrees with the observed initiation and termination times and distinctive slowness signature of the scattered waves and (2) it follows a scattering path analogous to previously observed $PK \cdot KP$ scattering.

Predicted Onset Time and Slowness of $P' \cdot d \cdot P'$

A strong argument for a $P' \cdot d \cdot P'$ scattering mechanism for the observed waves is the good agreement between the predicted and observed onset time and slowness of the waves. We determine the onset time and slowness of $P' \cdot d \cdot P'$ for a given source-receiver separation by raytracing PKP waves to a finely spaced grid of scatterers placed at a depth d in the upper mantle. Scattering to and from all branches of PKP (ab, bc, cd, and df) can potentially contribute to the observed wavetrain. However, the slowness images in Figures 3 and 4 show the dominant energy arrives with slownesses between 2.1 and 3.5 s/°, corresponding to the $PKPbc$ branch. This is consistent with the high theoretical and observed amplitudes of direct $PKPbc$ compared with other PKP branches (Bolt, 1968). Limiting our raytracing to $PKPbc$ slownesses produces good fits to the observed $P' \cdot d \cdot P'$ initiation time and slowness patterns as discussed in the following text.

The predicted onset time for $P' \cdot d \cdot P'$ for scattering depends on source depth and scattering depth, d, but interestingly it is independent of the source-receiver separation (Fig. 6). This behavior is also apparent from synthetic modeling of the scattered seismic wave field discussed later. The scattered ray path with the shortest travel time contains two PKP legs, each with a slowness corresponding to the b caustic ($PKPb$). Because the scattering can occur outside of the source-receiver diametrical plane, it is possible to connect two $PKPb$ legs from source-to-scatter and scatter-to-receiver at any source-receiver separation from 0° to 70° (the $P'P'b$ caustic). This results in the distance independent onset times for a given scattering depth plotted in Figure 6 (see also
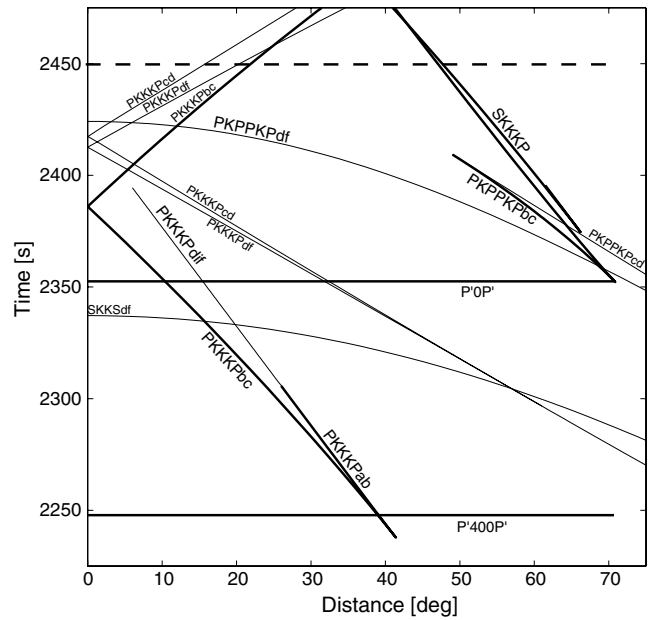
Figure 6. Theoretical onset time of $P' \cdot d \cdot P'$. The solid horizontal lines show the minimum travel time for $P' \cdot d \cdot P'$ waves scattered at the surface ($P' \cdot 0 \cdot P'$) and at 400 km below the surface ($P' \cdot 400 \cdot P'$) for the *iasp91* velocity model (Kennett and Engdahl, 1991). The dashed line shows the typical time for the scattered wave's amplitude to return to noise levels as can be seen in Figure 3.

Fig. 10). This $P' \cdot P'$ behavior is similar to the one described for $PK \cdot KP$ (Earle, 2002; Rost and Earle, 2010).

Figure 7 shows that the observed onset time of $P' \cdot d \cdot P'$ is consistent with scattering contributions from the upper 200 km of the Earth. It plots the predicted onset time for $P' \cdot d \cdot P'$ waves in the upper mantle at depths 200 km and 0 km superimposed on the array beams for highest signal-to-noise event B. A full listing of minimum $P' \cdot d \cdot P'$ arrival times is given in Table 2. The $P' \cdot d \cdot P'$ wave amplitude starts to increase at about 2300 s, which is consistent with an increase in scattering strength at 200 km depth. Accurately determining the depth extent of the fine-scale heterogeneity responsible for the scattered waves will require detailed
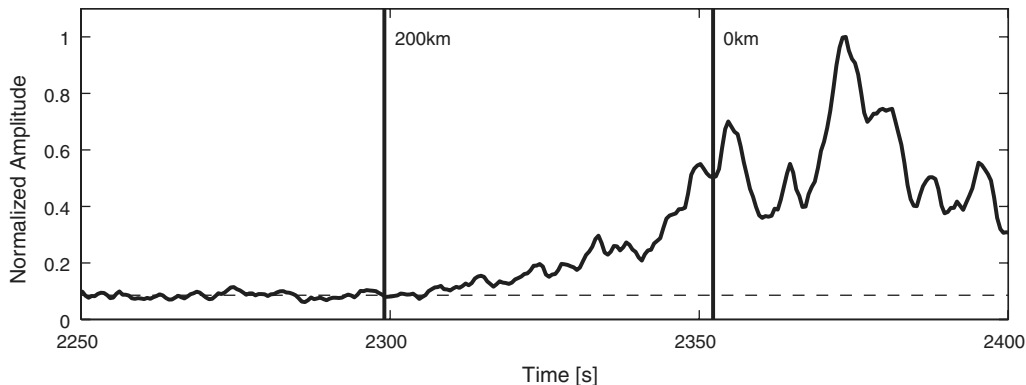
Figure 7. Beam of event B. Solid vertical lines show the minimum $P' \cdot d \cdot P'$ travel times for depths of 200, and 0 km below the surface for the *iasp91* velocity model (Kennett and Engdahl, 1991). The full minimum travel times for different depths throughout the mantle are given in Table 2. The beam shows an increase in wave amplitude starting at a time consistent with scattering from a depth of ~200 km.

Table 2
Minimum Travel Times for $P' \cdot d \cdot P'$ Scattered Phases
for Varying Scattering Depths

	IASP91*		PREM[†]	
Scattering Depth (km)	*PKP* Caustic Distance (°)[‡]	Minimum $P'dP'$ Travel Time (s)	*PKP* Caustic Distance (°)*	Minimum $P' \cdot d \cdot P'$ Travel Time (s)
0	144.57	2352.28	145.05	2353.48
200	144.10	2298.36	144.59	2300.36
400	143.54	2249.96	144.05	2252.28
600	142.84	2205.90	143.38	2208.40
800	141.99	2165.32	142.55	2167.90
1200	139.90	2087.58	140.49	2090.36
1600	137.23	2010.86	137.87	2014.08
2000	133.64	1932.54	134.44	1938.04
2400	128.62	1849.40	129.46	1854.36
2600	125.16	1803.38	126.14	1809.50
2800	120.40	1749.76	121.40	1756.14

*Velocity model from Kennett and Engdahl (1991).
[†]Preliminary Reference Earth Model from Dziewonski and Anderson (1981).
[‡]*PKPb* caustic distances are calculated for the appropriate scattering depth.

modeling of the scattering envelope that is beyond the scope of this paper. However, the predicted minimum onset times shown for $P' \cdot d \cdot P'$ indicate there is an increase in scattering strength above 200 km.

The most compelling evidence for a $P' \cdot d \cdot P'$ origin is the match between the predicted and observed double-peaked slowness pattern. Figure 8 shows the predicted $P' \cdot 0 \cdot P'$ slowness pattern, travel times, and scattering locations for source-receiver separations of 30°, 40°, and 50° for *PKPbc* to *PKPbc* scattering. The lower plots show, in global map view, the possible scattering locations for a hypothetical source (asterisk) and receiver (triangle) on the equator. The maps were generated by raytracing from the source to a 1°-by-1° grid of scattering locations on the surface and then to the receiver. It is not possible to connect two *PKPbc* legs to most of the grid points. These regions, shown in white, cannot produce any contribution to the scattered waves.

Only two modest-sized regions on the surface can contribute to the observed scattering envelope. In Figure 8, these regions lie on the 0° meridian and are color coded by the predicted $P' \cdot 0 \cdot P'$ travel time for waves scattering at that location. The two scattering regions result from symmetric scattering paths on each side of the source-receiver diametrical plane.

The upper plots of Figure 8 present the theoretical slownesses of $P' \cdot 0 \cdot P'$ scattered from the regions shown in the lower map-view plots. The distinctive off-azimuth slowness peaks seen in the data stacks of Figures 3 and 4 are clearly visible. However, in the data stacks generally one of the peaks is of larger amplitude than the other or sometimes falls below the noise level. This behavior is similar to $PK \cdot KP$ (Rost and Earle, 2010) and has been used to give constraints on lateral variations of the scattering strengths. Because the scatterers contributing to each peak arrive from geographically distinct regions, the asymmetric amplitude pattern is likely an indication of 3D variations in scattering strength, although resolving the scattering strength might be difficult.

Figure 9 shows the potential of $P' \cdot d \cdot P'$ to sample full mantle heterogeneity. We use a Monte-Carlo Phonon scattering algorithm (Shearer and Earle, 2004) to calculate the scattered wave field for different Earth models, including a 200-km-thick layer with 3% root mean square velocity variation (relative to the ambient mantle velocities at similar depth) and a correlation length of 4 km. We vary the depth of this layer between 600 and 1800 km (Fig. 9). The scattered $P' \cdot d \cdot P'$ energy is clearly visible as a band of energy with zero moveout with distance. The onset time of this energy varies according to the scattering depth as predicted. Energy from heterogeneities at depths smaller than 400 km might interfere with energy related to *PKKKP*, but could be separated using array techniques such as the ones used here.

Relation to $PK \cdot KP$ Scattering

The off-azimuth $P' \cdot d \cdot P'$ scattering path (Fig. 5) is remarkable, however, such a scattering geometry is not without precedent. Chang and Cleary (1981) document $PK \cdot KP$ waves in LASA data that travel an identical path to the $P' \cdot d \cdot P'$ waves, except they scatter at the underside of the CMB instead of in the upper mantle. Although these observations were originally attributed to scattering from topographic irregularities at the CMB (Chang and Cleary, 1981), raytracing shows contributions from fine-scale lower-mantle heterogeneity could also contribute to these observations (Earle, 2002; Rost and Earle, 2010). If we extend the concept of $P' \cdot d \cdot P'$ scattering from the Earth's surface to the CMB, $PK \cdot KP$ is simply a type of $P' \cdot d \cdot P'$ scattering with d equal to the thickness of the mantle.

Both $PK \cdot KP$ and $P' \cdot d \cdot P'$ are visible in several of the high signal-to-noise LASA events listed in Table 1. Figure 10 shows an array beam and slowness images for event J that includes $PK \cdot KP$, *PKKKP*, and upper-mantle $P' \cdot d \cdot P'$.
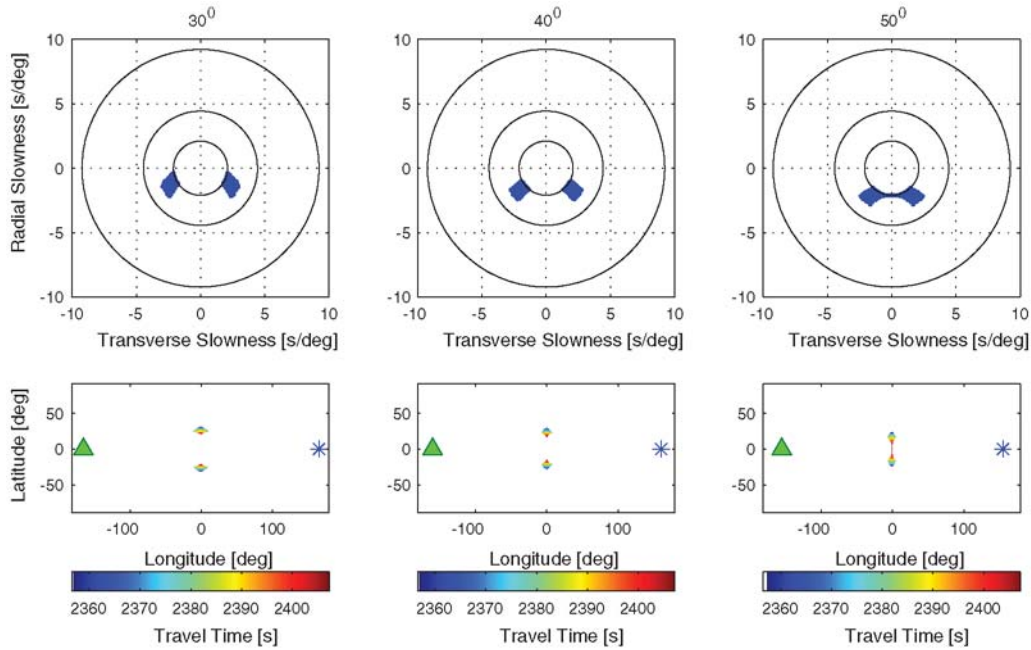
Figure 8. Predicted *P′•0•P′* slowness pattern, travel times, and scattering locations for source-receiver separations of 30°, 40°, and 50° for *PKPbc* to *PKPbc* scattering. The lower plots show the possible scattering locations in map view for a hypothetical source (asterisk) and receiver (triangle) on the equator. The scattering patches are color coded by the predicted *P′•0•P′* travel time for waves scattering at that location. The travel times for the surface scattering vary by ~20 s due to azimuthal variations. The upper plots show the theoretical slownesses of *P′•0•P′* scattered from the regions shown in the lower map-view plots. The distinctive off-azimuth slowness peaks as seen in the data stacks of Figures 3 and 4 are clearly visible.

The *PK•KP* and deep-mantle *P′•d•P′* arrivals are seen between 1735 and about 1950 s, the *PKKKP* energy arrives between 2260 and 2300 s, and the upper-mantle *P′•d•P′* arrive between 2320 and 2420 s. The deep-mantle *P′•d•P′* slowness image in Figure 10 (lower left) shows the characteristic two-peaked pattern, implying contributions from two distinct regions in the lowermost mantle or on the CMB.

The *PKKKP* slowness image (lower center) captures energy arriving at slownesses consistent with *PKKKPab* and *PKKKPbc*. *PKKKPab* arrives slightly off-azimuth (nonzero ρ_t), which is not unexpected for body waves traveling such a great distance. Furthermore, near-surface structure beneath the LASA station contributes to these mislocations (Engdahl and Felix, 1971; Iyer 1971). Although we aim to correct for these effects using the corrections proposed by Engdahl and Felix (1971), some travel-time variations between array stations due to local receiver structure remains. However, this deviation is much smaller than that observed for the *P′•d•P′* waves. The off-azimuth upper-mantle *P′•d•P′* waves are shown in the lower right slowness image. The difference in positive and negative ρ_t arrival amplitude likely arises from spatial variations in fine-scale upper-mantle heterogeneity.

The similarity between the observed slowness patterns in Figure 10 for deep- and upper-mantle *P′•d•P′* scattering indicates an analogous scattering mechanism. In addition, the agreement between ray-theoretical predictions and LASA observations of the scattered waves' initiation time and slowness support the scattering mechanism shown in Figure 5, which was first described by Chang and Cleary (1981).

Other Possible Scattering Source Regions

Although it is difficult to imagine that the agreement between the LASA observed initiation time and slowness pattern and those calculated for *P′•d•P′* is a coincidence, it is useful to exclude other possible source regions for the scattered waves before setting out to interpret observed patterns in these arrivals.

Given the off-azimuth arrival angle of the waves, one possible explanation might be scattering from isolated heterogeneity near the source or receiver and outside of the diametrical plane. However, if the isolated scatterers were near the source, they would not be detected in widely separated events such as events B and D. If the isolated scatterers were near the receiver, the observed slowness peaks in Figures 3 and 4 would have different values of (ρ_r, ρ_t) for events at different azimuths. Figures 3 and 4 show the peaks always occur near $(-2, 2)$ and/or $(-2, -2)$. This indicates the scattering geometry is the same or similar for the different events, but the scattering strength and therefore the amount of fine-scale heterogeneity varies geographically.

Inner-core heterogeneity demonstrated by Vidale and Earle (2000) is an unlikely source, given that waves traveling from scatterers in the inner core to LASA would have slownesses of 2.1 s/° or less, which is smaller than the observed
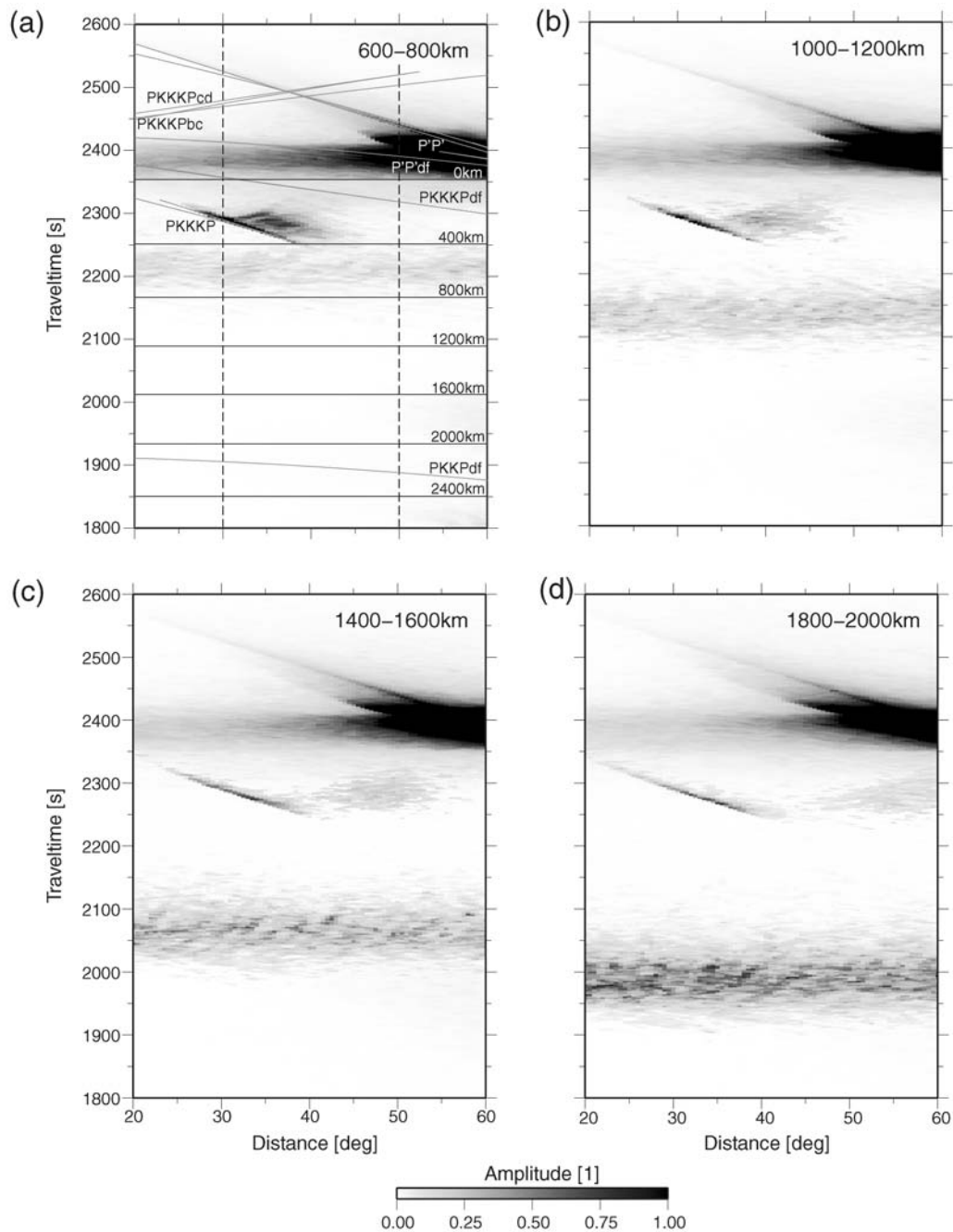
**Figure 9.** Phonon scattering synthetics (Shearer and Earle, 2004) of the $P' \cdot d \cdot P'$ wave field for different scatterer depths. (a) Synthetic wave field for a 200-km-thick scattering layer between 600 and 800 km depth. V_{RMS} variation is assumed to be 0.03 with a correlation length of 4 km. Travel-time curves of dominant arrivals in the time window are marked by gray lines. Horizontal gray lines indicate the minimum travel time of $P' \cdot d \cdot P'$ for depths of 0, 400, 800, 1200, 1600, 2000, and 2400 km. The synthetics show the constant travel time with distance of the onset of the scattered energy. (b) Same as (a) for a layer between 1000 to 1200 km depth. The scattered energy shows shorter travel times as shown in (a) as is predicted by the PKP_{bc} interpretation discussed in the text. The same scattering parameters as in (a) have been assumed. (c) Same as (a) for a scattering layer between 1400 and 1600 km depth. (d) Same as (a) for a scattering layer between 1800 to 2000 km.

values of about 2.8 s/°. Outer-core heterogeneity is unlikely given previous studies of the onset time of *PKPdf* precursors (Haddon and Cleary, 1974; Hedlin *et al.*, 1997) that preclude significant heterogeneity below the CMB.

The lower mantle contains fine-scale heterogeneity (Haddon, 1972), and possible contributions from this region

are more difficult to discount. To test for lower-mantle contributions, we calculated scattering envelopes using a Monte Carlo technique (Shearer and Earle, 2004). The method is useful for investigating whole Earth scattering because it preserves energy, includes multiple scattering, and accounts for all ray paths contributing significant energy to a given
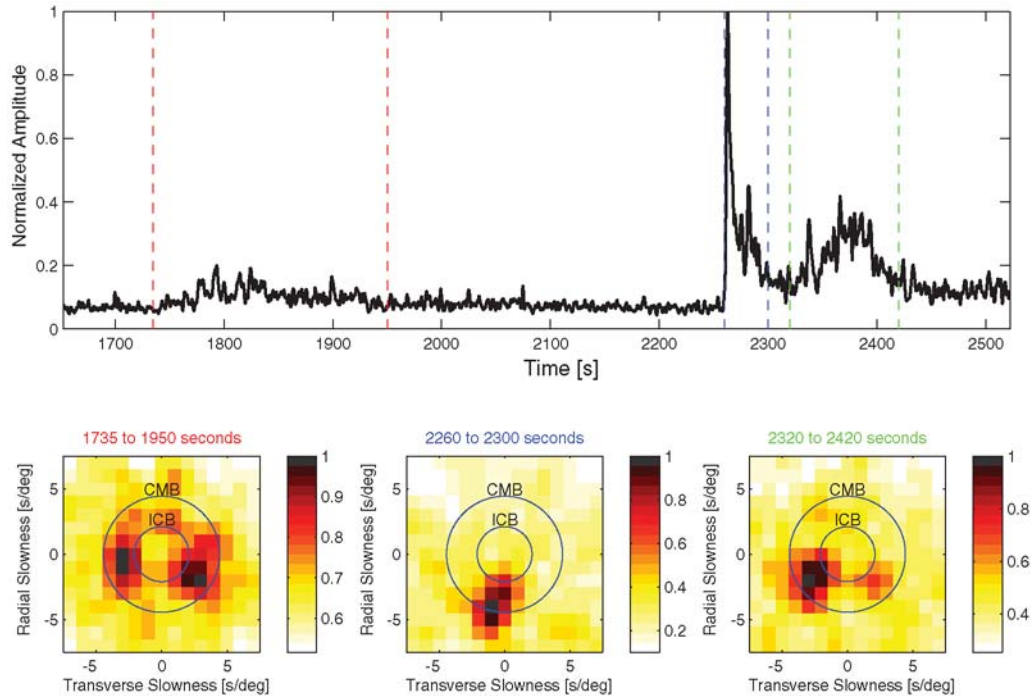
Figure 10. Array beam and slowness plots of *PKKKP* and *P′•d•P′* waves for event J. The lower slowness plots were made for time periods between the colored dashed lines. The time window between the dashed red lines (1735 to 1950 s) captures lower-mantle *P′•d•P′* waves, the window between the dashed blue lines (2260 to 2300 s) captures several branches of *PKKKP*, and the time window between the dashed green lines (2320 to 2420 s) brackets upper-mantle *P′•d•P′* waves. Note that slowness and back-azimuth deviations in these recordings are expected due to the complicated lateral variations in crustal structure beneath LASA (e.g., Greenfield and Sheppard, 1969; Iyer, 1971).

time-distance window. Scattering envelopes made for a model containing only lower-mantle and inner-core heterogeneity produced no significant energy arriving in the window 30° to 50° and 2250 s to 2450 s, where the upper-mantle *P′•d•P′* waves are observed, supporting an upper-mantle source for the observed scattered energy.

Discussion

The previous sections present observations of an undocumented scattered wavetrain arriving late in the high-frequency teleseismic wave field. It most likely originates from scattering of *PKPbc*-to-*PKPbc* in the Earth's crust and upper mantle with possible contributions from surface scattering near the bounce point. The waves belong to a family of scattered arrivals referred to here as *P′•d•P′*, where *d* represents the scattering depth, which can be at any depth in the mantle. Although detailed modeling of the physical properties of the heterogeneity responsible for the scattered waves is beyond the scope of this paper, we note there are several characteristics of *P′•d•P′* waves that have implications for future studies of fine-scale heterogeneity (Fig. 9).

Unlike *PKPdf* precursors, *P′•d•P′* waves observed near 45° sample the mantle unobstructed from the CMB to the surface. Figure 10 clearly images *P′•d•P′* waves scattering in the deep mantle (1735 to 1970 s) and upper mantle (2320 to 2420 s). *P′•d•P′* waves originating from scattering in the

midmantle would arrive between these wavetrains (Fig. 9) where no significant energy is seen for this event except the *PKKKP* arrival, which is absent in beams made at greater distances. The absence of observed midmantle *P′•d•P′* in Figure 10 does not exclude the possibility of fine-scale midmantle heterogeneity, because the arrivals may be below the noise level. However, future modeling of the observations will provide bounds on scattering strength throughout the entire depth of the mantle.

The *P′•d•P′* waves also indicate lateral variations of fine-scale mantle heterogeneity. The difference seen in the relative amplitude of the two *P′•d•P′* slowness peaks imaged in Figures 3 and 4 likely arises from differing amounts of heterogeneity in the two distinct patches of the upper mantle sampled by the waves (Fig. 8). The relative amplitude of the slowness peaks is geographically consistent. Without exception, the amplitude peak at negative transverse slowness is larger for all nine of the Aleutian events shown in Figure 2. Current work applying back-projection techniques to *P′•d•P′* waves is being conducted to map lateral variations of fine-scale heterogeneity throughout the entire mantle (Rost and Earle, 2010).

Data and Resources

The seismograms used in this paper were recorded by the Large Aperture Seismic Array (LASA), which operated

in Montana from 1968 to 1978. Most of the LASA recordings are lost, but rescued seismograms from this array can be requested from Paul Earle.

Acknowledgments

References

Bataille, K., and F. Lund (1996). Strong scattering of short-period seismic waves by the core-mantle boundary and the *P*-diffracted wave, *Geophys. Res. Lett.* **23,** 2413–2416.

Bolt, B. (1968). Estimation of PKP travel times, *Bull. Seismol. Soc. Am.* **58,** 1305–1324.

Chang, A. C., and J. R. Cleary (1981). Scattered PKKP: Further evidence for scattering at a rough core-mantle boundary, *Phys. Earth Planet. Inter.* **24,** 15–29.

Cormier, V. F. (1999). Anisotropy of heterogeneity scale lengths in the lower mantle from PKIKP precursors, *Geophys. J. Int.* **136,** 373–384.

Dainty, A. M. (1990). Studies of coda using array and three-component processing, *Pure Appl. Geophys.* **132,** 221–244.

Doornbos, D. J. (1974). Seismic wave scattering near caustics: Observations of PKKP precursors, *Nature* **247,** 352–353.

Dziewonski, A. M., and D. L. Anderson (1981). Preliminary reference Earth model, *Phys. Earth Planet. In.* **25,** 297–356.

Earle, P. S. (2002). Origins of high-frequency scattered waves near PKKP from Large Aperture Seismic Array data, *Bull. Seismol. Soc. Am.* **92,** 751–760.

Earle, P., and P. Shearer (1997). Observations of *PKKP* precursors used to estimate small-scale topography on the core-mantle boundary, *Science* **277,** 667–670.

Engdahl, E. R., and E. A. Flinn (1971). Nature of travel-time anomalies at LASA, *J. Geophys. Res.* **76,** 2706–2715.

Green, J., A. Frosch, and F. Romney (1965). Principles of an experimental Large Aperture Seismic Array (LASA), *Proc. IEEE* **53,** 1821–1833.

Greenfield, R. J., and R. M. Sheppard (1969). The Moho depth variations under the LASA and their effect on $dT/d\Delta$ measurements, *Bull. Seismol. Soc. Am.* **59,** 409–420.

Haddon, R. A. W. (1972). Corrugations on the CMB or transition layers between inner and outer cores?, *Eos Trans. Am. Geophys. Union* **53,** 600.

Haddon, R. A. W., and J. R. Cleary (1974). Evidence for scattering of seismic PKP waves near the mantle-core boundary, *Phys. Earth Planet. Inter.* **8,** 211–234.

Hedlin, R. A. W., P. S. Earle, and H. Bolton (2000). Old seismic data yield new insights, *Eos Trans. Am. Geophys. Union* **81,** 469.

Hedlin, M. A. H., P. M. Shearer, and P. S. Earle (1997). Seismic evidence for small-scale heterogeneity throughout the Earth's mantle, *Nature* **387,** 145–150.

Iyer, H. M. (1971). Variation of apparent velocity of teleseismic *P* waves across the large-aperture seismic array, Montana, *J. Geophys. Res.* **76,** 8554–8566.

Kanasewich, E. R. (1981). *Time Sequence Analysis in Geophysics*. third edition, The University of Alberta Press, Edmonton, 480 pp.

Kennett, B., and E. Engdahl (1991). Traveltimes for global earthquake location and phase identification, *Geophys. J. Int.* **105,** 429–465.

Margerin, L., and G. Nolet (2003). Multiple scattering of high-frequency seismic waves in the deep Earth: Modeling and numerical examples, *J. Geophys. Res.* **108,** 2234, doi 10.1029/2002JB001974.

Rost, S., and P. S. Earle (2010). Identifying regions of strong scattering at the core-mantle boundary from analysis of PKKP precursor energy. *Earth Planet. Sci. Lett.* **297,** 616–626.

Rost, S., and C. Thomas (2002). Array seismology: Methods and applications, *Rev. Geophys.* **40,** doi 10.1029/2000RG000100.

Rost, S., and C. Thomas (2009). Improving seismic resolution through array processing techniques, *Surv. Geophys.* **30,** 271–299.

Sato, H., and M. Fehler (1998). *Seismic Wave Propagation and Scattering in the Heterogeneous Earth*, Springer-Verlag, New York, 308 pp.

Shearer, P. M., and P. S. Earle (2004). The global short-period wavefield modeled with a Monte Carlo seismic phonon method, *Geophys. J. Int.* **158,** 1103–1117.

Tkalčić, H., M. Flanagan, and V. Cormier (2006). Observation of near-podal $P'P'$ precursors: Evidence for back scattering from the 150–220 km zone in the Earth's upper mantle, *Geophys. Res. Lett.* **33** L03305, doi 10.1029/2005GL024626.

Vidale, J. E., and P. S. Earle (2000). Fine-scale heterogeneity in the Earth's inner core, *Nature* **404,** 273–275.

U.S. Geological Survey
MS 966, Box 25046
DFC Denver, Colorado 80225
pearle@usgs.gov
        (P.S.E.)

School of Earth and Environment
Institute of Geophysics and Tectonics
University of Leeds
Woodhouse Lane, Leeds
LS2 9JT United Kingdom
s.rost@leeds.ac.uk
        (S.R.)

Institute of Geophysics and Planetary Physics
University of California–San Diego
La Jolla, California 92093-0225
pshearer@ucsd.edu
        (P.M.S.)

Institut für Geophysik
Universität Münster
Corrensstr. 24 48149
Münster, Germany
        (C.T.)